6

Optoelectronic Properties of ZnSe, ITO, TiO_2 and ZnO Thin Films

S. Venkatachalam[1], H. Nanjo[1], K. Kawasaki[1], H. Hayashi[1], T. Ebina[1] and D. Mangalaraj[2]
[1]*National Institute of Advanced Industrial Science and Technology*,
[2]*Department of Nanoscience and Technology, Bharathiar University*,
[1]*Japan*
[2]*India*

1. Introduction

Zinc selenide (ZnSe) a II-VI compound semiconductor with cubic zinc blende structure and a direct bandgap of 2.7 eV is found to be a very promising material for optoelectronic devices (Venkatachalam et al., 2007a). Semiconductor heterostructures employing zinc selenide and related alloys are an option for the production of optoelectronic devices emitting in the blue – green spectral range (Haase et al., 1991; Jeon et al., 1991). Nowadays there is a concentrated effort to produce high quality p-type zinc selenide based blue laser diodes (Drechsler et al., 1997; Fung et al., 1997). Particularly, Schottky photodiodes with fast response in the ultraviolet-visible range is more focused. Because Schottky barriers result in both very fast switching times and low forward voltage drop. The silicon photodiodes give more response in the infrared range; the main reason for this is the band gap value. The reported band gap value of Si is 1.1 eV. By providing an overlayer on the silicon surface, the silicon Schottky diodes give more response in the ultraviolet-visible range. Due to their direct energy gap in the visible range, zinc selenide would be perfectly suitable for this. The lattice mismatch, the difference in the thermal expansion coefficients, as well as the different chemical properties of zinc selenide and silicon (Si) are some of the sources of crystal defects generated at the interface between zinc selenide and silicon heterostructures. Zinc selenide has either a sphalerite structure with lattice parameter a = 5.668 Å or wurtzite structure with lattice parameters a = 3.820 Å and c = 6.626 Å. The lattice constant value of cubic silicon is reported as 5.6576 (JCPDS, 1990, card number 37). Usually, zinc selenide films were deposited onto gallium arsenide substrate, because of the high lattice match between zinc selenide and gallium arsenide (0.27 %). However, the production cost of gallium arsenide-based device is much higher than that of silicon. The lattice mismatch between zinc selenide and silicon is quite large (4.4 %) compared with gallium arsenide (0.27 %). However, in practice, the substrate strongly influences the nucleation and the mobility of the elements deposited on the substrate. In fact, the higher the substrate temperature, the higher the mobility of the deposited elements; therefore, the stoichiometric composition of zinc (Zn) and selenium (Se) in the zinc selenide film occurs at a sufficiently high substrate temperature (Chrisey & Hubler, 1994). A new PIN – like (Si (p)/ZnSe (n-)/ZnSe (n+)) visible photodiode was fabricated in 1996 using vapor phase epitaxy (Lour & Chang, 1996). They

used a two-step growth method in order to overcome the problem of lattice mismatch existing at the interface between zinc selenide and silicon. Zinc selenide-based silicon photodiode was recently fabricated (Ullrich, 1998). In order to bypass the lattice mismatch, the indium selenide (25Å) layer was used as a buffer layer between zinc selenide and silicon. These two techniques are very expensive. However, vacuum evaporation is very simple and inexpensive; it can be used for the deposition of film with large surface area. In this chapter, we investigate the effect of substrate temperature on the composition, structural, optical and electrical properties of vacuum evaporated zinc selenide thin films on silicon (100) and glass substrates at different substrate temperatures.

Indium-doped tin oxide (ITO) thin film is a wide band gap semiconductor with good conductivity and high optical transmission in the visible spectral range of 400 – 700 nm. Indium-doped tin oxide thin films are often used in a wide variety of applications, including solar cells and other optoelectronic devices. In recent years, metal oxide materials such as titanium dioxide and zinc oxide thin films have been extensively studied for various applications such as solar cells, gas sensors and protective coating (Feng et al., 2008). Among them, titanium dioxide is a very suitable oxide material for dye-sensitized solar cell (DSC) applications. Glass substrate can be used for solar cell applications, but glass is very brittle, and is too heavy, especially for large-area solar cell devices. These disadvantages can be overcome by using flexible substrates, which are lightweight and inexpensive. Optically transparent substrates with high glass transition temperature are desired for the above-mentioned applications. In addition, they need to withstand the growth conditions of metal oxides while maintaining their mechanical and optical properties. Particularly, the thermal resistant stability of flexible substrates should be maximal (~450°C). Because the anodized amorphous titanium dioxide can be changed into anatase titanium dioxide after the heat treatment in the range of 350-400°C (Lee et al., 2006). The deformation temperatures of polyethylene terephthalate and polycarbonate substrates were reported as 220 and 140°C, respectively (Wu & Chiou, 1997; Kim et al., 2001). Therefore, the polyethylene terephthalate and polycarbonate substrates could not be applied for the crystallization of amorphous titanium dioxide in the temperature range of 350-400°C. Recently, a very transparent flexible clay substrate was fabricated and it has more flexibility and high thermal resistance (Kawasaki et al., 2010). In the present work, titanium dioxide nanowires, nanorods and nanotubes are fabricated using hydrothermal and anodization method, respectively. In this chapter, we also report the surface morphology, photovoltaic and structural properties of titanium dioxide nanorods and nanotubes, which are prepared by hydrothermal method and electrochemical anodization method, respectively. The fabrication procedure of flexible dye-sensitized solar cells and the factors that affect the device performance will be discussed. Finally, the photovoltaic parameters of dye-sensitized solar cell based on titanium dioxide are compared with the dye-sensitized solar cell based on zinc oxide decorated titanium dioxide.

2. Experimental details

The appropriate weight zinc, selenium and iodine compounds were taken in an evacuated sealed quartz ampoule under a vacuum of 4×10^{-3} Pa. High purity zinc (99.999 %), selenium (99.999 %) and iodine (99.99 %) were used to prepare this zinc selenide compound. The zinc selenide compounds were prepared at 1148 K with iodine as a reactive agent. The prepared compound was yellow in colour. In the present work, the substrates are silicon (100) and

glass, which are used for the deposition of zinc selenide thin films. The silicon wafers were thoroughly rinsed with double distilled water and then treated with methanol for removing the organic impurities. The silicon substrates were then cleaned with trichloroethylene to break the organic molecules. Once again, the cleaned silicon substrates were treated with methanol. Finally, 48% hydrofluoric acid was used to remove the thin silicon dioxide layer on the silicon surface. The silicon wafers were inserted into the deposition chamber immediately after chemical cleaning. Pure aluminum (99.999 % Balzers, Switzerland) layer was deposited onto the back surface of silicon wafers by vacuum evaporation technique. Zinc selenide alloy was thermally evaporated from a molybdenum boat onto well-cleaned silicon (100) and glass substrates at different substrate temperatures (483 - 589 K) under a vacuum of 4×10^{-3} Pa, and gold was used as the top electrode. The completed device had an active area of about 2×10^{-6} m^2. In order to stabilize the deposited film, all the deposited films were annealed at 373 K for 30 minutes under a vacuum of 4×10^{-3} Pa. The composition of the film deposited onto glass substrate was studied using the Rutherford Backscattering spectrometry (RBS). In this case, 2 MeV He^+ ion beam was used for the experiment. The details of the experimental set-up could be found elsewhere (Jamieson, 1998). The structural analyses of the films were made by X-ray diffractrometer in the 2θ range from 20^o to 80^o. Optical transmission of zinc selenide films deposited onto micro glass glide was recorded using a ultraviolet-visible-near infrared spectrophotometer (CARY 2390). Electrical measurements were done in a rotary vacuum of 1.33 Pa at different temperatures (305 – 365 K) by using a cryostat equipped with a PT100 thermocouple. The capacitance values were measured using multifrequency LCR meter (4275HP). In the spectral response analysis, an Oriel 150 W Xenon Lamp was used as a light source, along with a monochromator from Acton Research Corporation. At each wavelength, the power P of the light incident on the gold mesa was carefully measured using a Newport 835 optical power meter that uses a UV-enhanced silicon photodiode (818UV) as the detector.

3. Results and discussion

3.1 Optoelectronic properties of zinc selenide (ZnSe) thin films

A typical Rutherford backscattering spectrum for a film deposited at a substrate temperature of 553 K is shown in Fig. 1. The edge of the overlapping bands corresponding to the elements zinc and selenium are seen as well as those corresponding to silicon in the silicon substrate. The collected Rutherford backscattering spectra (Red Line) were then fitted by code Rump (Doolittle, 1985) to find the relative concentrations of various elements in the film. Spectra similar to this are obtained for other deposited films. The average ratio of the deposited films is found to be (ZnSe) $I_{0.001}$. The composition is found to be nearly stoichiometric and the percentage of iodine is minimal. Figure 2 shows the X-ray diffraction patterns of zinc selenide thin films grown on silicon (100) substrates at different substrate temperatures. Only one peak of zinc selenide and two peaks of silicon are observed. It is observed that the X-ray diffraction patterns of all the films show a most preferred orientation along (111) plane. The (111) direction is the close-packing direction of the zinc blende structure and all the deposited films are polycrystalline having cubic zinc blende structure. The (111) peak for the films deposited at T_s = 483 K is broad and very weak. It may be due to the mixed phase of amorphous and crystalline in Zn – Se bonding in zinc selenide thin films. The X-ray diffraction intensity of (111) peak increases and the peak becomes narrower as the substrate temperature is increased from 483 to 589 K.

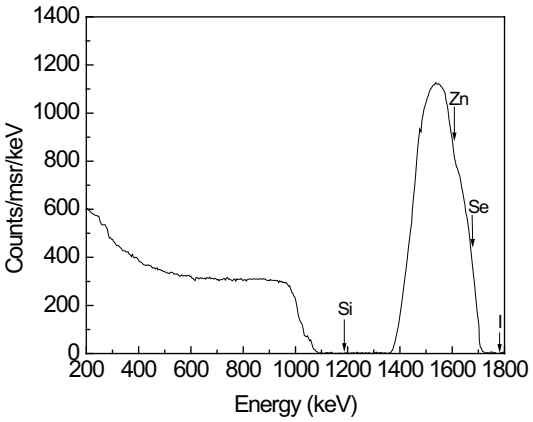

Fig. 1. Rutherford backscattering spectrum of vacuum evaporated zinc selenide thin film deposited at a substrate temperature of 553 K. [Reprinted with permission from (Venkatachalam et al., 2006). Copyright @ IOP Publishing Ltd (2006)].

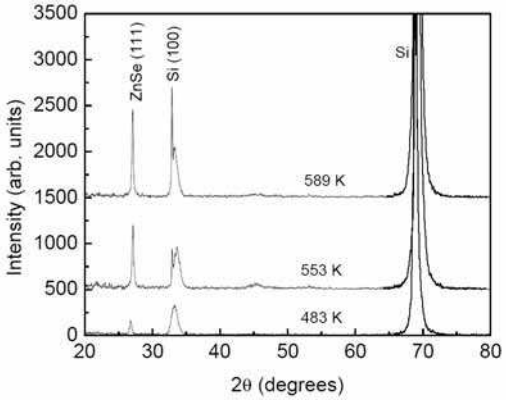

Fig. 2. X-ray diffraction patterns of zinc selenide thin films deposited on silicon substrate at different substrate temperatures. [Reprinted with permission from (Venkatachalam et al., 2006). Copyright @ IOP Publishing Ltd (2006)]

The particle size (D) is calculated using Debye - Scherrer's formula from the full width at half maximum (β) (Warren, 1990). The particle size values are calculated as 22, 36 and 41 nm at 483, 553 and 589 K, respectively. The best films (characterized by lower value of full width at half maximum and higher value of particle size) are obtained with the growth temperature between 553 and 589 K. The lattice constant values are calculated as 5.72, 5.678 and 5.6785Å at 483, 553 and 589 K, respectively. If we compare these values with the reported value of bulk a_{ZnSe} (5.6684 Å) (JCPDS #37-1463), the calculated lattice constant value for the film deposited at 483 K is larger than that of reported value. However, the lattice constant values are very close to the reported value for the films deposited at 553 and 589 K. This result suggests that the deposited zinc selenide thin film at 483 K is strongly

affected by the two dimensional compressive stress at the ZnSe/Si interface in the growth plane, in order to accommodate the lattice misfit. But the compressive stress shows a decreasing trend at the higher substrate temperature (553 and 589 K).

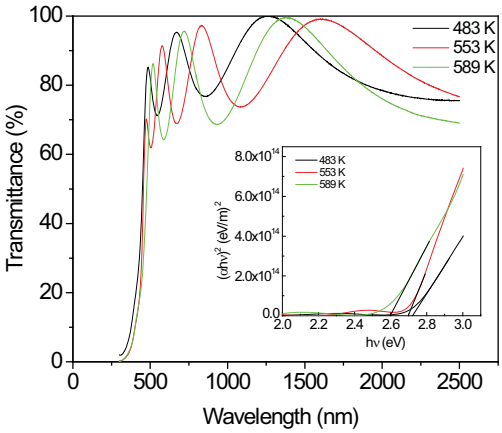

Fig. 3. Transmittance spectra of zinc selenide thin films deposited at different substrate temperatures. [Reprinted with permission from (Venkatachalam et al., 2006). Copyright @ IOP Publishing Ltd (2006)].

The transmittance spectra of the zinc selenide thin films deposited at different substrate temperatures are shown in Fig. 3. This sharp fall of transmittance occurs in the lower wavelength region corresponding to the band gap of the film. The optical band gap (E_g) values are calculated as 2.72, 2.69 and 2.60 eV for 483, 553 and 589 K, respectively. The energy band gap value decreases from 2.72 to 2.6 eV as the substrate temperature is increased from 483 to 589 K and all the films are found to have direct allowed transition. The calculated optical band gap values are in good agreement with the bulk reported value (2.7 eV) (Venkatachalam et al., 2007b).

The ZnSe/p-Si heterojunction prepared at 553 K is studied using current – voltage and capacitance – voltage characteristics. Figure 4 shows a typical plot of I – V characteristics of ZnSe /p-Si Schottky diodes in forward and reverse biases measured at different temperatures. This I – V characteristics follow the standard diode equation (Rakhshani et al., 1998) for forward bias below ≈ 0.4 V as given by

$$\left[I = I_0[\exp(qV / nkT) - 1] \right] \tag{1}$$

where n is called the ideality factor, q is the electronic charge, k is the Botzmann constant and T is the temperature.

The ideality factor is evaluated from the plot between Ln I vs. V [inset of Fig. 4] and is found to be in the range from 2.01 to 3.51. Compared with previous reports (Montes & Herino, 2000), the calculated value of ideality factor is low. In general when the ideal diffusion current is the dominating factor, then the value of the ideality factor n will be equal to 1, whereas this value equal to 2 when the recombination current is the dominating factor (Sze, 1985). However, in the present case the value of ideality factor is greater than 2. The departure of the ideality factor from unity may be due to the fact that the Schottky barrier

contains an interfacial layer on the silicon surface. However, in the present work, we could not observe any interfacial layer on the silicon surface (Fig.5). Figure 5 shows the high-resolution transmission electron microscopy (HRTEM) image of a ZnSe/Si heterostructures, which reveals a clear interface between substrate (silicon) and overlayer (zinc selenide layer). The main reason is the existence of a laterally varying potential barrier height, caused by a non-uniform interface.

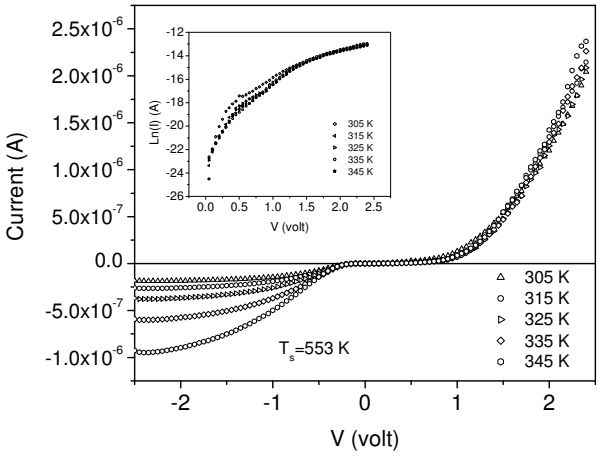

Fig. 4. Forward and reverse current versus voltage characteristics of ZnSe/Au Schottky diode. The inset of Fig.4 shows the plot of voltage versus LnI. [Reprinted with permission from (Venkatachalam et al., 2006). Copyright @ IOP Publishing Ltd (2006)].

The reverse bias characteristics would be controlled by the generation-recombination and band–to- band tunneling mechanisms at small (up to -0.4 V) and large bias, respectively, which might be the reason for a small kink at –0.4 V (Chiang & Bedair, 1985). The plot between the measured values of capacitance and voltage for ZnSe / p-Si diodes is shown in Fig. 6a. We obtained a straight line by plotting a curve between $1/C^2$ versus V, which implies a similar behaviour for an abrupt heterojunction (Khlyap & Andrukhiv, 1999). The intercept of this plot at $1/C^2 = 0$ corresponds to the built-in potential V_{bi}, and is found to be 1.51 V. The value of barrier height (Singh et al., 1993; Pfister et al., 1977) can be calculated from the measured value of V_{bi}.

$$\phi_{Bn} = V_{bi} + V_n + \frac{kT}{q} \tag{2}$$

where $V_n = kT/q$. Ln (N_v/N_A), k is the Boltzmann constant, T is the temperature, q is the charge of the electron, N_v is the density of states in the valence band and N_A is the effective carrier concentration. From the slope of the $1/C^2$ versus voltage plot, the value of effective carrier concentration is calculated as 3.55×10^{19} $(m^2/F)^2$ / V. The calculated values of barrier height and acceptor concentration (N_A) are calculated as 1.95 eV and 4.37×10^{11} cm^{-3}, respectively. The spectral photoresponse of the device prepared at 589 K is shown in Fig. 6b. It shows a very good photoresponse in the UV-Visible range. The quantum efficiency for the device prepared at 553 and 589 K is calculated as 0.25 and 0.1 %, respectively.

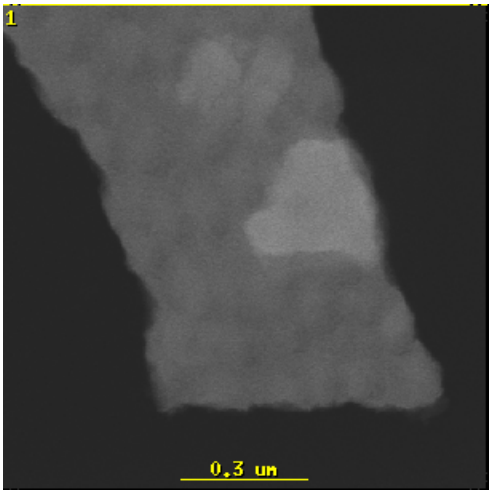

Fig. 5. High-resolution transmission electron microscopy image of the prepared ZnSe/p-Si Schottky diodes. [Reprinted with permission from (Venkatachalam et al., 2006). Copyright @ IOP Publishing Ltd (2006)].

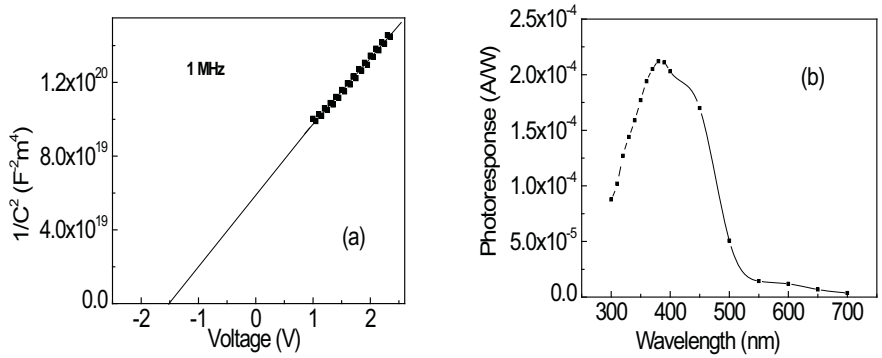

Fig. 6. Dependence of $1/C^2$ value on applied voltage (a) and spectral photoresponse (b) of ZnSe/p-Si Schottky diode. [Reprinted with permission from (Venkatachalam et al., 2006). Copyright @ IOP Publishing Ltd (2006)].

3.2 Preparation and characterization of indium-doped tin oxide thin films

Nanocrystalline indium-doped tin oxide (ITO) thin films were prepared on glass and clay substrates by ion beam sputter deposition method. Preparation and deposition parameters of nanocrystalline indium-doped tin oxide thin films were found elsewhere (Venkatachalam et al., 2010). The scanning electron microscope (SEM) images show that the surface morphology of indium-doped tin oxide thin film on glass substrate is smooth (Fig. 7a); in contrast, the surface morphology of indium-doped tin oxide thin film on clay substrate is rough (Fig. 7b). The inset of Figure 7b shows the flexibility of indium-doped tin oxide thin film coated clay substrate. Flexibility of indium-doped tin oxide thin film coated clay substrate is estimated as 17 mm, from a diameter of curvature. X-ray diffraction patterns of annealed indium-doped tin oxide thin film are

shown in Fig. 8; the X-ray diffraction patterns showed two different orientations, i.e., (400) and (222) on different substrates, i.e., glass and clay, respectively. The sheet resistances of indium-doped tin oxide thin film on glass (32 Ω/□) is lower than that on clay (41 Ω/□); it is due to the difference in substrate surface roughness between ITO/glass and ITO/clay.

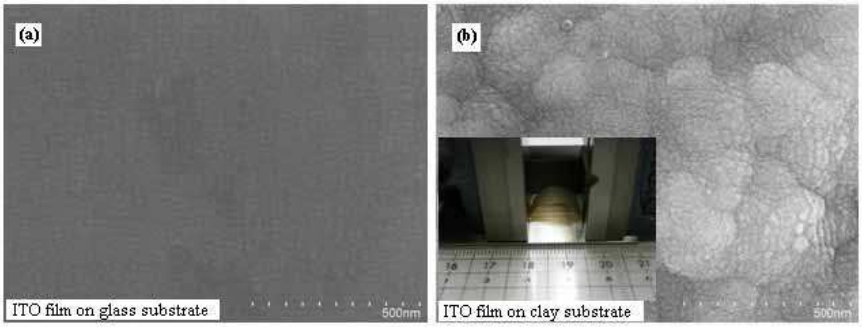

Fig. 7. Scanning electron microscope images of indium tin oxide thin films (inset Fig. 7b shows photograph of flexible ITO/Clay substrate). [Reprinted with permission from (Venkatachalam et al., 2011) Copyright @ The Japan Society of Applied Physics (2011)].

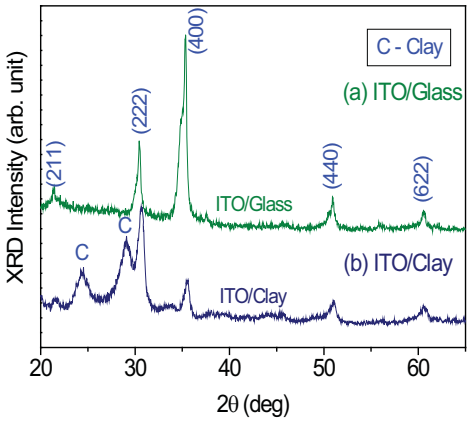

Fig. 8. X-ray diffraction patterns of annealed indium tin oxide thin films. [Reprinted with permission from (Venkatachalam et al., 2011) Copyright @ The Japan Society of Applied Physics (2011)].

3.3 Preparation and characterization of nanostructured titanium dioxide films

The hydrothermal synthesis of titanium dioxide (TiO_2) film was carried out in a Teflon-lined stainless steel autoclave. In a typical synthesis process, titanium n-butoxide (1.0 ml) was used with hydrochloric acid (20 ml) and deionized water (40 ml). The reaction time and temperature were fixed at 17 h and 160°C, respectively. Scanning electron microscope images of as-prepared titanium dioxide films on indium-doped tin oxide and fluorine-doped tin oxide (FTO) films coated glass substrates are shown in Fig. 9. It shows that the surface morphology of titanium dioxide films on indium-doped tin oxide substrate indicates

the existence of many uniform, dandelion-like structures with diameter in the range of 6-7 μm (Fig. 9a). A selected area of high magnification image (inset of Fig.9a) shows that each dandelion-like structure is composed of nanorods with an average diameter of 150 nm. It is attributed that if there is no lattice match between titanium dioxide and indium-doped tin oxide substrate, the titanium dioxide initially nucleates as islands and then the nanorods grow from these islands to form dandelion-like morphology. In contrast, the surface morphology of titanium dioxide films on fluorine-doped tin oxide substrate (Fig. 9c) shows that the whole surface is composed of ordered titanium dioxide nanorods with square top facets. The cross-sectional view (inset of Fig.9c) confirms that the growth of the titanium dioxide nanorods is along the direction perpendicular to the fluorine-doped tin oxide substrate. This shows that titanium dioxide thin film grows epitaxially on fluorine-doped tin oxide substrate; it is due to the small lattice mismatch (~ 2 %) between titanium dioxide and fluorine-doped tin oxide films, because fluorine-doped tin oxide films and titanium dioxide films have similar crystal structure. The length and size of the nanorods are evaluated as 3.9 μm and 150 nm, respectively.

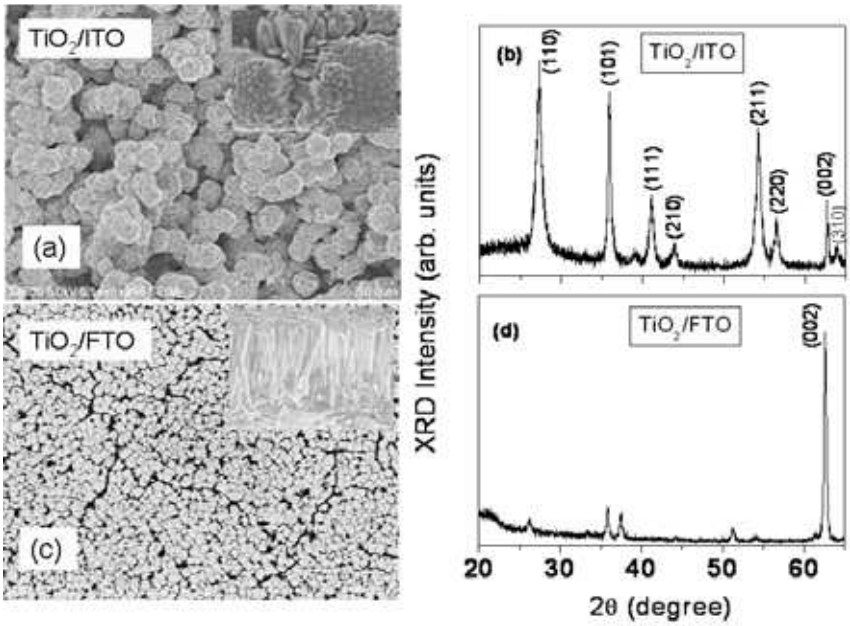

Fig. 9. Scanning electron microscope images and X-ray diffraction patterns of titanium dioxide films on different substrates; (a and b) TiO_2 film on ITO/glass, (c and d) TiO_2 film on FTO/glass.

Figure 9b shows the X-ray diffraction pattern of titanium dioxide films prepared on indium-doped tin oxide substrate. A very strong rutile peak is observed at 2θ of 27.37°, assigned to (110) plane. Other rutile peaks are observed at 2θ of 36.10° (101), 41.26° (111), 44.01° (210), 54.36° (211), 56.59° (220), 62.92° (002) and 64.10° (310). In contrast, titanium dioxide film on fluorine-doped tin oxide shows a preferred orientation in the (002) direction (Fig. 9d), as indicated by strong characteristic peak at 2θ of 62.92°. Here, the absence of (110), (111) and

(211) peaks indicate that the nanostructured titanium dioxide film is highly oriented with respect to the substrate surface and the titanium dioxide nanorods grow in the (002) direction with the growth axis parallel to the substrate surface normal (Bang & Kamat, 2010).

After preparing the freestanding nanostructured titanium dioxide films, it is transferred from a glass substrate onto an indium-doped tin oxide film coated transparent flexible clay substrate. The photograph of freestanding layer of titanium dioxide prepared by hydrothermal method is shown in Fig. 10a; it can be easily handled with tweezers. Figure 10b shows the scanning electron microscope images of freestanding titanium dioxide layer. The size of the nanorod is calculated as 150 nm. A very thin layer of titanium dioxide paste is used between the freestanding titanium dioxide and indium-doped tin oxide film coated flexible clay (LiSA-TPP) substrate in order to improve the adhesion. The freestanding titanium dioxide layer deposited on flexible ITO/clay substrate is used as an anode. The platinum sputtered indium-doped tin oxide film coated flexible clay/mica substrate is used as a counter electrode. Surlyn spacer film with a thickness of 60 μm is used as a spacer. The completed device had an active area of 0.5 cm^2. From the photocurrent density-voltage characteristic, the open circuit voltage, short circuit current and fill factor are calculated as 0.51 V, 1.14 mA and 56 %, respectively. However, the efficiency of the prepared device is less than 1 %. It is considered that the adhesion layer restricts the flow of electrons from titanium dioxide photoelectrode into the collector (ITO) (Park et al., 2011).

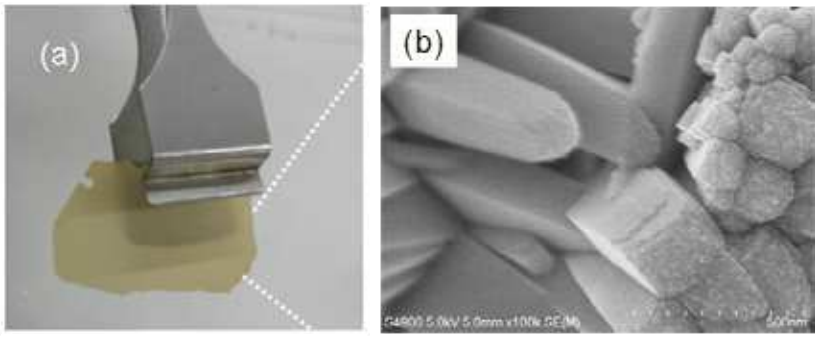

Fig. 10. SEM images and photograph of freestanding TiO_2 layer.

3.4 Preparation of titanium dioxide nanotube arrays and titanium dioxide nanowire covered titanium dioxide nanotube arrays on titanium foil and plate

Nanostructured titanium dioxide films were prepared by anodization of titanium foil and plate at room temperature. The anodization was performed in ethylene glycol containing 2 vol.% H_2O+ 0.3 wt.% ammonium fluoride (NH_4F) for different anodization time. The anodized titanium sample was then annealed in air at 400°C for an hour. Figure 11(a-d) shows top and bottom-side view scanning electron microscope images of anodized titanium plate and foil. It clearly shows the formation of well-ordered titanium dioxide nanotube arrays on both titanium plate and foil. The bottom side-views of the tube layer (Figs. 11c and d) reflects an uneven morphology. At the bottom, the tubes are closely packed together. The diameter and length of titanium dioxide nanotube arrays on Ti plate are calculated as 100 nm and 5.6 μm, respectively.

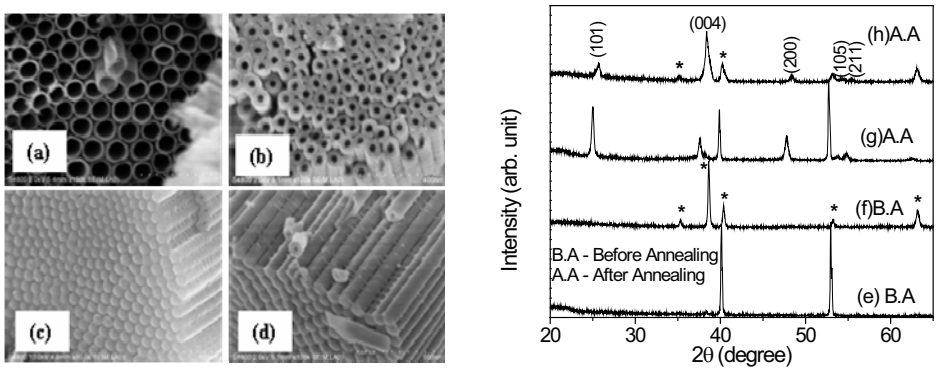

Fig. 11. Scanning electron microscope images [Top views (Ti plate (a); foil (b)) and bottom side views (Ti plate (c); foil (d))] and XRD patterns [Ti plate (e and g) and Ti foil (f and h)] of anodized Ti plate and Ti foil.

Figure 11(e-h) shows the X-ray diffraction patterns of anodized titanium plate and Ti foil before and after annealing. In Fig. 11e and f, the X-ray diffraction peaks at 35.3, 38.64, 40.4, 53.2 and 63.18 correspond to titanium. This is attributed that the as-prepared titanium dioxide is amorphous before annealing; only titanium peaks are seen (Fig.11e and f). In order to change the amorphous titanium dioxide into anatase titanium dioxide, anodized titanium sample was annealed in air at 400°C for an hour. After annealing, the amorphous titanium dioxide has been changed into crystalline with a more preferred orientation along (101) direction. The particle size values of titanium dioxide on titanium plate and titanium foil are calculated as 41 and 24 nm, respectively. The calculated lattice parameters of TiO_2/Ti plate and TiO_2/foil coincide well with the reported value of bulk titanium dioxide (a=3.7822Å) (JCPDS #21-1272). The stress in the TiO_2/Ti plate is tensile. On the other hand, the TiO_2/Ti foil is under compressive stress (see Table 1).

Sample code	Anodization Time	2θ	FWHM (degree)	Lattice parameter (a) (Å)	Stress (%)
TiO2/Ti plate	240 min	25.00	0.209	3.804	0.57
TiO2/Ti foil	180 min	25.63	0.360	3.761	-0.56

Table 1. Structural parameters of anodized Ti plate and foil.

Figure 12A and D shows the scanning electron microscope images of titanium dioxide nanowires covered titanium dioxide nanotube arrays prepared by anodization method. The nanotubes divided into several parts are observed near the mouth (Fig.12C). The electrochemical etching causes the divided nanotubes to further split into several parts that lead to the formation of nanowires. Figure 12B shows that titanium dioxide nanotube arrays with diameter of 100 nm exist underneath the nanowires.

Figure 13 shows the photocurrent density-voltage characteristics of dye-sensitized solar cells based on titanium dioxide nanotube arrays and nanoparticles. Under backside illumination, the short-circuit current density and power conversion efficiency of dye-sensitized solar cells based on titanium dioxide nanotube arrays are much higher than that of P25 (see Table

2). Similar results have been observed by (Tao et al., 2010). This result shows that the main factor responsible for the enhancement of the short circuit current is the improvement of electron transport and electron lifetime in titanium dioxide nanotube arrays. This increased light-harvesting efficiency in titanium dioxide nanotube-based dye-sensitized solar cell could be a result of stronger light scattering effects that leads to significantly higher charge collection efficiencies of nanotube-based dye-sensitized solar cells relative to those of nanoparticles-based dye-sensitized solar cells (Jennings et al., 2008). The dye-sensitized solar cells device performance under backside illumination is very low. This is attributed that the backside illumination affects the light absorption capacity of the dyes, because the I_3^- electrolyte cuts the incident light in the wavelength range of 400 – 650 nm.

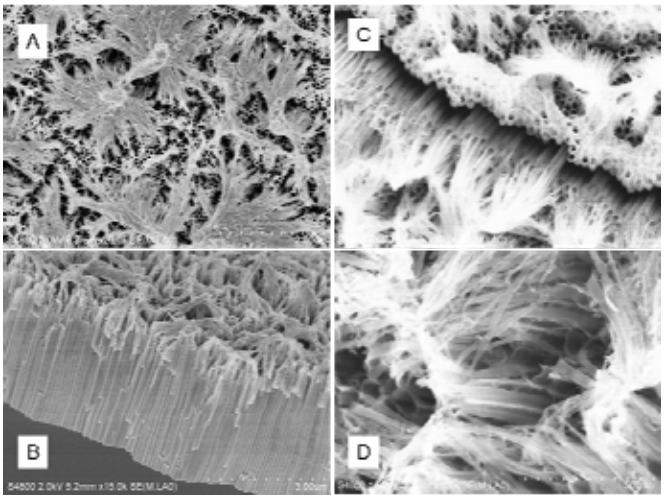

Fig. 12. Scanning electron microscope images of anodized Ti foil and Ti plate. Top views of Ti foil (A) and plate at low (C) and high magnification (D)]; cross-sectional view of Ti foil (B).

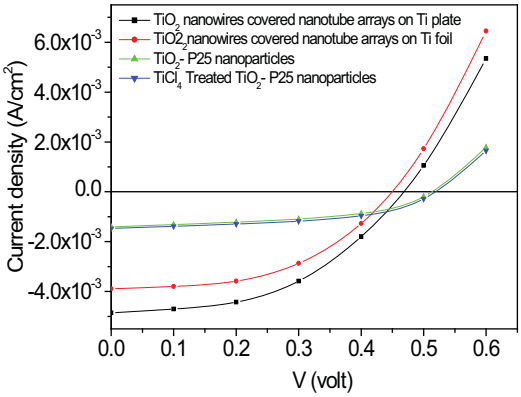

Fig. 13. Photocurrent density-voltage characteristics of dye-sensitized solar cells based on TiO_2 nanotube arrays and nanoparticles.

Sample code	Anodization Time (min)	V_{oc} (V)	J_{sc} (mA/cm²)	FF	Efficiency (%)
Sample 1 (Ti Plate)	240	0.470	4.85	0.463	1.06
Sample 2 (Ti Foil) (Film thickness=3μm)	180	0.450	3.85	0.493	0.854
Sample 3 [TiO_2(P25)] (Film thickness=2μm)		0.518	1.4	0.522	0.23
Sample 4 [TiO_2(P25)+$TiCl_4$] (Film thickness=2μm)		0.523	1.5	0.499	0.391

Table 2. Photovoltaic parameters of dye-sensitized solar cells based on titanium dioxide nanotube arrays and P25 films.

3.5 Preparation of titanium dioxide nanotube arrays on indium-doped tin oxide and silicon substrates

From the previous results, we observed that the use of foil and plate limits their potential applications, particularly in the fabrication of solar cells. An alternative approach is the preparation of nanostructured titanium dioxide films on transparent conducting glass substrate by anodization method. In the electrochemical anodization process, the substrate temperature, lattice mismatch between the substrate and film, and film thickness affect the properties of the films; because of which the anodization process is affected (Sadek et al., 2009). (Wang & Lin, 2009) reported that the formation of titanium dioxide nanotube arrays were not only affected by electrolytes and applied potential, but also affected by electrolyte temperature. Recently, titanium dioxide nanotube array films were successfully prepared by anodization of as-prepared ion-beam sputtered titanium thin films at low electrolyte temperature (5°C) and the key parameter to achieve the titanium dioxide nanotube arrays is the electrolyte temperature (Macak et al., 2006). In the present work, the titanium dioxide nanotube arrays are successfully prepared by anodization of as-prepared ion-beam sputtered titanium films at room temperature. Titanium thin films were deposited on indium-doped tin oxide and silicon substrates by ion beam sputter deposition method at room temperature. The acceleration voltage supplied to main gun was fixed at 2500 V. Pure Ar was employed as the sputtering gas. Nanostructured titanium dioxide thin films were prepared by electrochemical anodization method. The Ti/ITO/glass was anodized in glycerol containing 2.5 vol. % H_2O+0.5 wt.% NH_4F at an applied potential of 30 V for the anodization time of 240 min. On the other hand Ti/Si sample was anodized in ethylene glycol containing 2.0 vol. % H_2O + 0.3wt. % NH_4F at an applied potential of 20 V for 180 min. Nanostructured titanium dioxide thin films are formed by anodization using a two electrode configuration with Ti film as an anode and platinum as a cathode.

Generally, the formation mechanism of the titanium dioxide nanotube array films is proposed as two competitive processes, electrochemical oxidation and chemical dissolution. From these results, we observed that no titanium dioxide nanotubes, but titanium dioxide nanoholes were formed for anodization time of 60 min (Figure not shown). It shows that the titanium dioxide nanohole array films are easily formed during the short-time of anodization. Titanium dioxide nanotube arrays can also be prepared on the titanium film surface, but this can be accomplished by increasing the anodization time; this is due to the

high chemical dissolution at the inter-pore region. These results clearly show that high dissolution rate at the inter-pore region is very important in order to get the ordered nanotube arrays. Figure 14 shows the top-view scanning electron microscope images of titanium film anodized in different electrolytes at 30 and 20 V for anodization time of 240 and 180 min, respectively. It can be found that the pore growth and formation of titanium dioxide nanotube arrays on the titanium film surface are uniformly distributed. Scanning electron microscope images confirm the formation of titanium dioxide nanotubes on indium-doped tin oxide coated glass and silicon substrates. The growth rate and diameter of the titanium dioxide nanotube arrays prepared in ethylene glycol containing electrolyte is larger than that in glycerol containing electrolyte. The film thickness is calculated as 400 nm. In order to change the amorphous titanium dioxide into anatase titanium dioxide, the as-prepared titanium dioxide nanotube array film was annealed in air at 350ºC for an hour. The annealed titanium dioxide electrode is used for preparing the dye-sensitized solar cell device. The platinum-coated indium-doped tin oxide substrate is used as a counter electrode. The photovoltaic parameters such as open circuit voltage (V_{oc}), short-circuit current density (J_{sc}) and fill factor (FF) are calculated as 0.432 V, 1.58 mA/cm^2 and 0.36, respectively. The low value of fill factor is attributed to the large value of series resistance at the interface between titanium dioxide and indium-doped tin oxide films. The efficiency of the prepared device is less than 1 %. In this method, the film thickness is one of the disadvantages for DSC applications. Because the amount of dye adsorption can be increased by increasing the internal surface area as well as the thickness of the films.

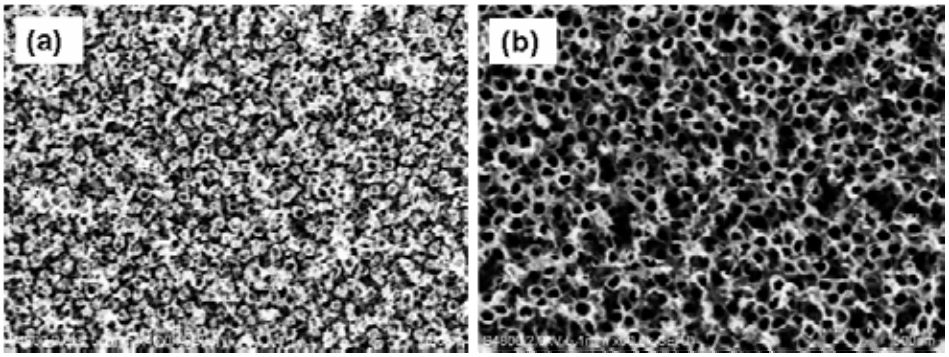

Fig. 14. SEM images of Ti/ITO/glass and Ti/Si after anodization in glycerol containing 2.5 vol. % H_2O + 0.5wt. % NH_4F at 30 V and ethylene glycol containing 2.0 vol. % H_2O + 0.3wt. % NH_4F at 20 V for 240 min (a) and 180 min (b), respectively.

3.6 Preparation and characterization of zinc oxide nanorods on different substrates

There are many reports about fabrication and characterization of dye-sensitized solar cells. However, the review results suggest that the recombination rate of the injected photoelectrons in dye-sensitized solar cell based on titanium dioxide electrode is very high compared to zinc oxide decorated titanium dioxide electrode, it is due to the absence of an energy barrier at the electrode to electrolyte interface. In the present work, we study the effect of growth conditions on the surface morphological and structural properties of zinc oxide films. We also investigate the photovoltaic performance of dye-sensitized solar cells based on titanium dioxide and titanium dioxide decorated with zinc oxide nanoparticles.

Finally, discussion on possible factors that improve the dye-sensitized solar cell device performance, because two different kinds of photoelectrodes have been used in this study. Nanostructured zinc oxide paste was prepared by using hydrothermal method. In order to study the effect of substrates surface condition on the surface morphological properties of zinc oxide, zinc oxide films were also prepared on different substrates such as indium-doped tin oxide film coated flexible clay, glass, zinc plate and copper wire substrates. Nanocrystalline indium-doped tin oxide films were prepared on clay and glass substrates by ion beam sputter deposition method (Venkatachalam et al., 2011). The hydrothermal synthesis of zinc oxide paste and films were carried out in a Teflon-lined stainless steel autoclave. In a typical synthesis process, zinc chloride (40 ml) was used with 2 ml of ammonia solution.

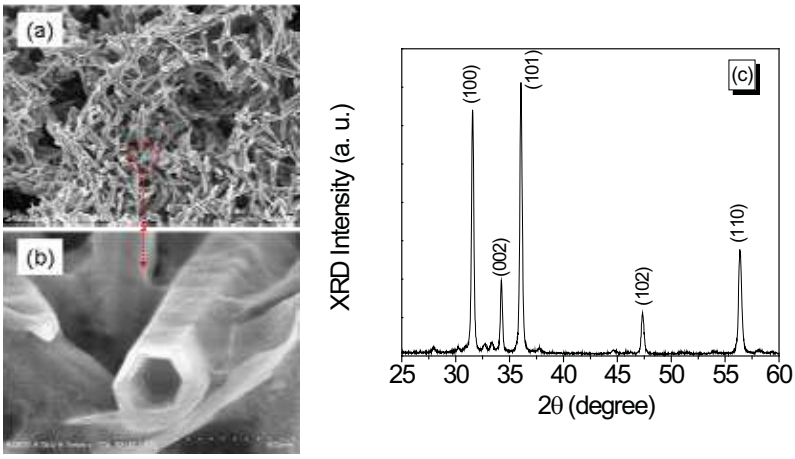

Fig. 15. Scanning electron microscope images of ZnO paste at low magnification (a) and high magnification (b); XRD pattern of ZnO paste prepared by hydrothermal method (c).

Figure 15 shows the scanning electron microscope images and X-ray diffraction pattern of zinc oxide paste prepared by hydrothermal method. The surface morphology (Fig. 15a) of as-prepared zinc oxide paste clearly shows the formation of zinc oxide nanorod like structure which are uniformly distributed throughout the surface of the sample. The formation of hexagonal shaped zinc oxide nanotube is clearly shown in Fig. 15b. The formation mechanism of the porous zinc oxide nanotube is mainly due to the preferential etching along the c-axis and slow etching along the radial directions. The X-ray diffraction peaks at 2θ of 31.9°, 34.76°, 36.3°, 47.6° and 56.68°arise from the (100), (002), (101), (102) and (110) hexagonal planes. All the X-ray diffraction peaks match well with the wurtzite zinc oxide structure with lattice constants of a =3.25 Å and c= 5.16 Å (Wang et al., 2008). It shows that the zinc oxide nanotubes have good crystallinity, exhibiting a hexagonal structure. The presence of very weak intensity of the (002) in the X-ray diffraction pattern (Fig. 15c) supports the formation of zinc oxide tubular structure. Similar results have been observed by (Wang et al., 2008).

Figure 16A and B shows the scanning electron microscope images of zinc oxide films prepared on indium-doped tin oxide film coated glass and clay substrates. The diameters of zinc oxide nanorods on both clay and glass substrates are not uniform; they are in the range

from hundred to several hundred nanometers. The size of the zinc oxide nanorod on clay substrate is larger than that on glass substrate. The growth parameters of zinc oxide films on both glass and clay were same. The substrate surface roughnesses of indium-doped tin oxide film deposited on glass and clay were calculated by AFM. The substrate surface roughnesses of ITO/glass and ITO/clay are calculated as 4.3 and 83 nm, respectively. The substrate surface of ITO/clay is much larger than that of ITO/glass. This is attributed that the substrate surface roughness strongly influences the growth rate of zinc oxide films. X-ray diffraction pattern for zinc oxide film grown on glass shows a main peak at $2\theta=34.76°$, it corresponds to (002) orientation of hexagonal zinc oxide. In contrast, the zinc oxide film deposited on clay shows a main peak at $2\theta = 32.08°$, it corresponds to (100) plane. X-ray diffraction patterns show two different orientations i.e., (002) and (100) on different substrates (glass and clay) (figure not shown). The exact reason, which determines the crystal growth and orientation, is the difference in substrate surface roughness between the glass and clay. Figure 16C and D shows the scanning electron microscope images of zinc oxide nanorods synthesized by hydrothermal method on copper and zinc substrates. The zinc oxide nanorods on both copper and zinc substrates are vertically oriented and well aligned (Fig. 16C and D). It also reveals that the nanorods are grown in a very high density. Scanning electron microscope images clearly show that the morphology of the final product is strongly dependent on the substrate surface condition.

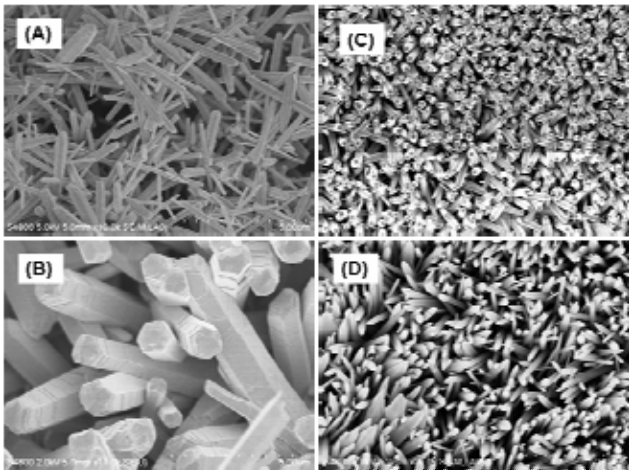

Fig. 16. Scanning electron microscope images of zinc oxide nanorods prepared on different substrates; (A) ITO/glass, (B) ITO/clay, (C) copper wire and (D) zinc plate.

The titanium dioxide paste was coated on indium-doped tin oxide coated glass substrate by doctor blade method. At first, the titanium dioxide coated ITO sample was annealed in air at 150°C for 30 min. Then the annealed TiO_2/ITO samples were placed into the zinc oxide solution for 30 sec. Finally, all the samples were annealed in air at 400°C for 2 h. The titanium dioxide film thicknesses are calculated as 1.5 and 3 μm. In the present work, we employed a very thin layer of titanium dioxide film (1.5 or 3 μm) in order to check the effect of zinc oxide on the performance of the dye-sensitized solar cells. Finally, all the titanium dioxide electrodes were immersed into the ethanol solution containing ruthenium (N-719) dye. Then the dye-anchored titanium dioxide electrodes were rinsed with ethanol solution and then dried in air.

Figure 17 shows the photocurrent density-voltage characteristics of dye-sensitized solar cells based on titanium dioxide nanoparticulate film and zinc oxide decorated titanium dioxide films. The short circuit density of titanium dioxide based dye-sensitized solar cell is lower than that of dye-sensitized solar cell based on zinc oxide decorated titanium dioxide (see Table 3). This is attributed that the titanium dioxide electrode introduces charge recombination that mainly occurs at the electrode/electrolyte, so that the open circuit voltage and fill factor values are low compared to zinc oxide decorated titanium dioxide, this is due to the absence of energy barrier layer (Wang et al., 2009). The performance of the dye-sensitized solar cell based on zinc oxide decorated titanium dioxide has been improved; because the photogenerated electrons are more effectively extracted and, thereby, open circuit voltage (V_{oc}), short-current density (J_{sc}) and fill factor (FF) increase together. This is attributed that the protection of titanium dioxide surface with additional zinc oxide layer is considered to be another possible reason for the improved efficiency in zinc oxide decorated titanium dioxide photoanode. This result indicates that the power conversion efficiency of dye-sensitized solar cell based on zinc oxide decorated titanium dioxide can be increased by increasing the titanium dioxide film thickness.

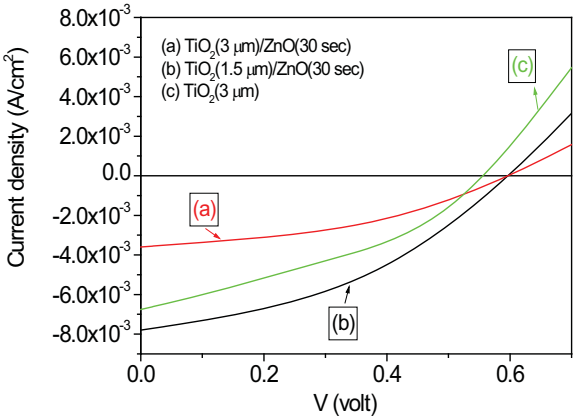

Fig. 17. Photocurrent density-voltage characteristics of dye-sensitized solar cell based on TiO_2 and ZnO/TiO_2 films.

Photoelectrode	**TiO_2(P25) Thickness**	**V_{oc} (V)**	**J_{sc} (mA/cm²)**	**FF**	**η (%)**
ZnO(30sec)/TiO_2	1.5 μm	0.606	3.60	0.41	0.9
ZnO(30sec)/TiO_2	3.0 μm	0.606	7.80	0.42	2.0
TiO_2	3.0 μm	0.560	6.75	0.35	1.32

Table 3. Photovoltaic parameters of dye-sensitized solar cell based on ZnO/TiO_2 and TiO_2 photoelectrodes.

4. Conclusions

The zinc selenide thin films were deposited on Si and glass substrates by vacuum evaporation method at different substrate temperatures (483, 553 and 589K). All the films were polycrystalline and showed the cubic zinc blende structure with a preferred orientation along

the (111) direction. In the optical studies, the band gap value decreased from 2.72 to 2.60 eV as the substrate temperature was increased from 483 to 589 K. In the current–voltage studies, the departure of the ideality factor from unity was due to the existence of a laterally varying potential barrier height, caused by a non-uniform interface. From the capacitance–voltage study, the examined heterostructures are abrupt heterojunctions. Indium-tin oxide thin films were deposited on clay and glass substrates by ion beam sputter deposition method at room temperature. The flexibility of indium doped tin oxide coated clay substrate was measured as 17 mm. The as-deposited indium doped tin oxide coated films on flexible clay substrate showed low sheet resistance (41 Ω/□) and high optical transmittance (~80%). Titanium dioxide nanorods were prepared on indium doped tin oxide coated glass and fluorine doped tin oxide coated glass substrates by hydrothermal method. The titanium dioxide nanorods were grown perpendicular to the fluorine doped tin oxide substrate; it was attributed to epitaxial growth of titanium dioxide films. Finally, flexible dye-sensitized solar cell was successfully fabricated. The titanium dioxide nanotube arrays and nanowires covered titanium dioxide nanotube arrays were successfully prepared by electrochemical anodization method. In this case, the dye adsorption capacity and power conversion efficiency of dye-sensitized solar cells based on nanowire covered titanium dioxide nanotube arrays were much higher than that of dye-sensitized solar cells based on titanium dioxide nanotube arrays. The titanium films were deposited on indium doped tin oxide coated glass substrate. The titanium dioxide nanotube arrays were successfully prepared on titanium films at room temperature. Nanostructured zinc oxide films were successfully deposited on different substrates by hydrothermal method. X-ray diffraction study clearly showed that the crystal quality and orientation of the final products were strongly dependent on the experimental parameter. Scanning electron microscope images showed that the shape and size of the nanorods could be perfectly generated by controlling the substrate surface roughness. The efficiency of ZnO/TiO_2 based DSC significantly improved from 0.9 to 2 % as the titanium dioxide film thickness was increased from 1.5 to 3μm. It showed the positive role of zinc oxide coating that leads to the improvement of the efficiency. This result indicated that the zinc oxide coating on the titanium dioxide surface suppresses the recombination at the TiO_2/dye/electrolyte interface. The power conversion efficiency could be increased by increasing the TiO_2 film thickness.

5. References

Bang, J.H.; Kamat, P.V. (2010). Solar Cell by Design. Photoelectrochemistry of TiO_2 Nanorod Arrays Decorated with CdSe. *Adv. Funct. Mater.* Vol.20, (June 2010), pp.1970-1976, ISSN 1616-3028

Chiang, P. K.; Bedair, S. M. (1985). P-n junction formation in InSb and $InAs_{1-x}Sb_x$ by Metalorganic chemical vapor deposition. *Appl. Phys. Lett.* Vol. 46, (February 1985), pp. 383-385, ISSN 1077-3118

Chrisey, D.B.; Hubler, G.K. (1994). *Pulsed Laser Ablation and Deposition of Thin Films*, John Wiley, ISBN: 978-0-471-59218-1, New York

Doolittle, L. R. (1985). Algorithms for the rapid simulation of Rutherford backscattering spectra. *Nucl. Instrum. Meth. B*, Vol. 9, (June 1985), pp. 344-351, ISSN 0969-8051

Drechsler, M. ; Meyer, B.K.; Hofmann, D. M.; Ruppert, P.; Hommel, D. (1997). Optically detected cyclotron resonance properties of high purity ZnSe epitaxial layers grown on GaAs. *Appl. Phys. Lett.* Vol. 71, (August 1997), pp. 1116-1117, ISSN 1077-3118

Fung, K.K. ; Wang, N.; Sou, I.K. (1997). Direct observation of stacking fault tetrahedra in ZnSe/GaAs(001) pseudomorphic epilayers by weak beam dark-field transmission

electron microscopy. *Appl. Phys. Lett.* Vol. 71, (September 1997), pp. 1225-1228, ISSN 1077-3118

Feng, X.; Shankar, K.; Varghese, O.K.; Paulose, M.; Latempa, T.J. (2008). Single crystal TiO_2 nanowire arrays grown directly on transparent conducting oxide coated glass: synthesis details and applications. *Nano Lett.* Vol. 8, No. 11, (October 2008), pp. 3781-3786, ISSN 1530-6984

Haase, M.A.; Qiu, J.; DePuydt, J. M.; Cheng, H. (1991). Blue-green laser diodes. *Appl. Phys. Lett.* Vol. 59, (September 1991), pp. 1272-1274, ISSN 1077-3118

Jennings, J.R.; Ghicov, A.; Peter, L.M.; Schmuki, P.; Walker, A.B. (2008). Dye-Sensitized Solar Cells Based on Oriented TiO_2 Nanotube Arrays: Transport, Trapping, and Transfer of Electrons. *J Am. Chem. Soc.* Vol. 130, No. 40, (September 2008), pp. 13364-13372, ISSN 0002-7863

Jeon, H. ; Ding, J. ; Patterson, W. ; Nurmikko, A.V. ; Xie, W. ; Grillo, D.C. ; Kobayashi, M. ; Gunshor, R.L. (1991). Blue-green injection laser diodes in (Zn,Cd)Se/ZnSe quantum wells. *Appl. Phys. Lett.* Vol. 59, (December 1991), pp. 3619-3621, ISSN 1077-3118

Jamieson, D. N. (1998). Structural and electrical characterisation of semiconductor materials using a nuclear microprobe. *Nucl. Instrum.Meth. B*, Vol. 136, (March 1998), pp. 1–13, ISSN 0969-8051

Khlyap, G.; Andrukhiv, M. (1999). New Heterostructures n-PbS/n-ZnSe: Long-Term Stability of Electrical Characteristics. *Cryst. Res. Technol.* Vol. 34, No. 5-6, (June 1999), pp. 751-756, ISSN 1521-4079

Kim, H.; Horwitz, J. S.; Kushto, G.P.; Kafafi, Z.H.; Chrisey, D.B. (2001). Indium tin oxide thin films grown on flexible plastic substrates by pulsed-laser deposition for organic light-emitting diodes. *Appl. Phys. Lett.* Vol. 79, No.3, (July 2001), pp. 284-286, ISSN 1077-3118

Kawasaki, K.; Ebina, T.; Tsuda, H.; Motegi, K. (2010). Development of flexible organo saponite films and their transparency at high temperature. *Appl. Clay Sci.* Vol. 48, (March 2010), pp. 111-116, ISSN 0169-1317

Lour, W-S.; Chang, C.-C. (1996). VPE grown ZnSe/Si PIN-like visible photodiodes. *Solid State Electron.* Vol. 39, (September 1996), pp. 1295-1298, ISSN 0038-1101

Lee, W. J.; Alhoshan, M.; Smyrl, W.H. (2006). Titanium dioxide nanotube arrays fabricated By anodizing processes. *J Electrochem. Soc.* Vol. 153, (September 2006), pp. B499-505, ISSN 00134651

Montes, L.; Herino, R. (2000). Luminescence and structural properties of porous silicon with ZnSe intimate contact. *Mater. Sci. Eng. B*, Vol. 69-70, (January 2000), pp. 136–141, ISSN 0921-5107

Macak, J.M.; Tsuchiya, H.; Berger, S.; Bauer, S.; Fujimoto, S.; Schmuki, P. (2006). On wafer TiO_2 nanotube-layer formation by anodization of Ti-films on Si. *Chem. Phys. Lett.* Vol.428, (September 2006), pp. 421-425, ISSN 0009-2614

Pfister, G.; Melnyk, A. R.; Scharfe, M. E. (1977). Enhancement of hole drift velocity in amorphous As_2Se_3 by iodine doping Original Research Article. *Solid State Commun.* Vol. 21, No. 9, (March 1977), pp. 907-910, ISSN 0038-1098

Park, H.; Kim, W.-R.; Jeong, H.-T. ; Lee, J.-J. ; Kim, H.-G. ; Choi, W.-Y. (2011). Fabrication of dye sensitized solar cells by transplanting highly ordered TiO_2 nanotube arrays. *Sol. Energy Mater. Sol. Cells*, Vol. 95, No. 1, (January 2011), pp. 184-189, ISSN 0927-0248

Rakhshani, A. E.; Makdisi, Y.; Mathew, X.; Mathews, N. R. (1998). Charge Transport Mechanisms in Au–CdTe Space-Charge-Limited Schottky Diodes. *Phys. Status Solidi a*, Vol. 168, (July 1998), pp. 177-187, ISSN 1862-6319

Sze, S. M. (2nd Eds.). (1985). *Semiconductor Devices, Physics and Technology*, John Wiley, ISBN 0-471-33372-7, New York

Singh, A.; Cova, P.; Masut, R. A. (1993). Energy density distribution of interface states in Au Schottky contacts to epitaxial $In_{0.21}Ga_{0.79}As$:Zn layers grown on GaAs by metalorganic vapor phase epitaxy. *J Appl. Phys.* Vol. 74, (December 1993), pp. 6714-6719, ISSN 0021-8979

Sadek, A.A.; Zheng, H.; Latha, K.; Wlodarski, W.; Kalantar-zadeh, K. (2009). Anodization of Ti thin film deposited on ITO. *Langmuir*, Vol.25, (November 2009), pp. 509-514, ISSN 0743-7463

Tao, R-H.; Wu, J-M.; Xue, H-X.; Song, X-M.; Pan, X.; Fang, X-Q.; Fang, X-D.; Dai, S-Y. (2010). A novel approach to titania nanowire arrays as photoanodes of back-illuminated dye sensitized solar cells. *J Power Sources*, Vol. 195, (May 2010), pp. 2989-2995, ISSN 0378-7753

Ullrich, B. (1998). Comparison of the photocurrent of ZnSe/InSe/Si and ZnSe/Si heterojunctions. *Mater. Sci. Eng. B*, Vol. 56, (October 1998), pp. 69 -71, ISSN 0921-5107

Venkatachalam, S.; Mangalaraj, D.; Narayandass, Sa. K. (2006). Influence of substrate temperature on the structural, optical and electrical properties of zinc selenide (ZnSe) thin films. *J Phys. D: Appl. Phys.* Vol. 39, (November 2006), pp. 4777-4782, ISSN 1361-6463

Venkatachalam, S. ; Agilan, S. ; Mangalaraj, D. ; Narayandass, Sa.K. (2007a). Optoelectronic properties of ZnSe thin films. *Mat. Sci. Semicon. Proc.* Vol. 10, (July 2007), pp. 128-132, ISSN 1369-8001

Venkatachalam, S.; Mangalaraj, D.; Narayandass, Sa.K.; Velumani, S.; Schabes-Retchkiman, P.; Ascencio, J.A. (2007b). Structural studies on vacuum evaporated ZnSe/p-Si Schottky diodes. *Mater. Chem. Phys.* Vol. 103, (June 2007), pp. 305-311, ISSN 0254-0584

Venkatachalam, S.; Iida, Y.; Kanno, Y. (2008). Preparation and characterization of Al doped ZnO thin films by PLD. *Superlattices and Microstructures*, Vol. 44, No.1, (July 2008), pp. 127-135, ISSN 0749-6036

Venkatachalam, S.; Nanjo, H.; Hassan, F.M.B.; Kawasaki, K.; Kanakubo, M.; Aizawa, T.; Aida, T.; Ebina, T. (2010). Characterization of nanocrystalline Indium Tin Oxide thin films prepared by ion-beam sputter deposition method. *Thin Solid Films*, Vol. 518, (September 2010), pp. 6891-6896, ISSN 0040-6090

Venkatachalam, S.; Nanjo, H.; Hassan, F.M.B.; Kawasaki, K.; Wakui, Y.; Hayashi, H.; Ebina, T. (2011). Properties of Indium Tin Oxide Thin Films Deposited on Glass and Clay Substrates by Ion-Beam Sputter Deposition Method. *Jpn. J Appl. Phys.* Vol. 50, (January 2011), pp. 01AK03-1-01AK03-4, ISSN 1347-4065

Wu, W.F.; Chiou, B.S. (1997). Deposition of indium tin oxide films on polycarbonate substrates by radio-frequency magnetron sputtering. *Thin Solid Films*, Vol. 298, No. 1-2, (April 1997), pp. 221-227, ISSN 0040-6090

Warren, B. E.; X-ray Diffraction; Dover: New York; 1990, p 253.

Wang, H.; Li, G.; Jia, L.; Wang, G.; Tang, C. (2008). Controllable Preferential-Etching Synthesis and Photocatalytic Activity of Porous ZnO Nanotubes. *J Phys. Chem. C*, Vol. 112, No. 31, (July 2008), pp. 11738-11743, ISSN 1932-7455

Wang, J.; Lin, Z. (2009). Anodic Formation of Ordered TiO Nanotube Arrays: Effects of Electrolyte Temperature and Anodization Potential. *J Phys. Chem. C*, Vol.113, (February 2009), pp.4026-4030, ISSN 1932-7455

Wang, M.; Huang, C.; Cao, Y.; Yu, Q.; Deng, Z.; Liu, Y.; Huang, Z.; Huang, J.; Huang, Q.; Guo, W.; Liang, J. (2009).Dye-sensitized solar cells based on nanoparticle-decorated ZnO/TiO_2 core/shell nanorod arrays. *J Phys. D: Appl. Phys.* Vol. 42, (2009), pp. 155104, ISSN 1361-6463

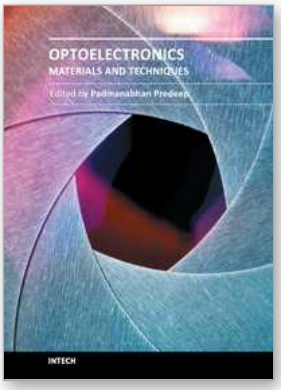

Optoelectronics - Materials and Techniques

Edited by Prof. P. Predeep

ISBN 978-953-307-276-0
Hard cover, 484 pages
Publisher InTech
Published online 26, September, 2011
Published in print edition September, 2011

Optoelectronics - Materials and Techniques is the first part of an edited anthology on the multifaceted areas of optoelectronics by a selected group of authors including promising novices to the experts in the field. Photonics and optoelectronics are making an impact multiple times the semiconductor revolution made on the quality of our life. In telecommunication, entertainment devices, computational techniques, clean energy harvesting, medical instrumentation, materials and device characterization and scores of other areas of R&D the science of optics and electronics get coupled by fine technology advances to make incredibly large strides. The technology of light has advanced to a stage where disciplines sans boundaries are finding it indispensable. Smart materials and devices are fast emerging and being tested and applications developed in an unimaginable pace and speed. Here has been made an attempt to capture some of the materials and techniques and underlying physical and technical phenomena that make such developments possible through some real time players in the field contributing their work and this is sure to make this collection of essays extremely useful to students and other stake holders such as researchers and materials scientists in the area of optoelectronics.

How to reference

In order to correctly reference this scholarly work, feel free to copy and paste the following:

S. Venkatachalam, H. Nanjo, K. Kawasaki, H. Hayashi, T. Ebina and D. Mangalaraj (2011). Optoelectronic Properties of ZnSe, ITO, TiO2 and ZnO Thin Films, Optoelectronics - Materials and Techniques, Prof. P. Predeep (Ed.), ISBN: 978-953-307-276-0, InTech, Available from: http://www.intechopen.com/books/optoelectronics-materials-and-techniques/optoelectronic-properties-of-znse-ito-tio2-and-zno-thin-films

INTECH
open science | open minds

InTech Europe
University Campus STeP Ri
Slavka Krautzeka 83/A
51000 Rijeka, Croatia
Phone: +385 (51) 770 447
Fax: +385 (51) 686 166
www.intechopen.com

InTech China
Unit 405, Office Block, Hotel Equatorial Shanghai
No.65, Yan An Road (West), Shanghai, 200040, China
中国上海市延安西路65号上海国际贵都大饭店办公楼405单元
Phone: +86-21-62489820
Fax: +86-21-62489821